RSC Advances

PAPER

View Article Online
View Journal | View Issue

Cite this: *RSC Adv.*, 2026, **16**, 16748

Catalytic ignition of the [BMIM]DCA-H_2O_2 propellant with the $Cu(vim)_2(DCA)_2$ complex

Yuqi Zhang,[ab] Yuan Yao,[bc] Peihao Dou,[b] Qing Cheng*[ab] and Yanqiang Zhang *[ac]

An ionic liquid (IL)-H_2O_2 propellant offers a green alternative to the traditional hydrazine-N_2O_4 system. Due to the weak oxidizing ability of H_2O_2, typical ILs cannot be spontaneously ignited. To address this issue, catalytic ignition was proposed, and a series of metal complex catalysts with the formula $M(vim)_2(DCA)_2$ (M = Mn, Fe, Co, and Cu) were synthesized. Single-crystal X-ray diffraction analysis shows that the Mn, Fe and Co complexes adopt an octahedral geometry, while the Cu complex exhibits a planar quadrilateral geometry. The physicochemical properties (T_d, ΔH_c, ΔH_f, and I_{sp}) of the fuels (10 wt% $M(vim)_2(DCA)_2$ + 90 wt% [BMIM]DCA) were evaluated. Dynamic light scattering and UV-vis spectroscopy analyses confirm that the four complexes disperse well in [BMIM]DCA. Ignition tests reveal that $Cu(vim)_2(DCA)_2$ exhibits the best catalytic performance for the ignition of [BMIM]DCA with H_2O_2, achieving t_{id} as short as 21 ms. EPR studies indicate that $Cu(vim)_2(DCA)_2$ catalyzes H_2O_2 to generate reactive oxygen species (·OH, $\cdot O_2^-$, and $^1O_2$), which subsequently induce the spontaneous ignition of [BMIM]DCA. DFT calculations reveal that the zero-dimensional geometry of $Cu(vim)_2(DCA)_2$ features an unsaturated Cu center and electron-rich ligand framework. This typical structure enables efficient electron transfer to activate H_2O_2, boosting ROS generation and ignition. This work clarifies the crucial role of the metal center in the IL-H_2O_2 system and provides an important insight into the catalytic ignition of the "double-green" propellants.

Received 12th January 2026
Accepted 13th March 2026

DOI: 10.1039/d6ra00294c

rsc.li/rsc-advances

Introduction

Propellants serve as the power source for spacecraft and are crucial for deep-space exploration. Conventional hydrazine-N_2O_4 propellants offer high energy density and specific impulse.[1,2] However, they are flammable, highly carcinogenic, and corrosive during storage, transport, and operation.[3–5] In 1990, the International Green Propellant Working Group was established to guide the development of sustainable propellants.[6] Combining ionic liquids (ILs) with hydrogen peroxide (H_2O_2) represents a promising candidate for double-green propellants. ILs possess low volatility and high structural tunability,[7–9] while H_2O_2 acts as a clean oxidizer.[10,11] The IL-H_2O_2 propellants meet the key requirements for sustainable propulsion systems. This combination allows precise control of the fuel-oxidizer ratio and provides stable thrust.[12,13]

The IL-H_2O_2 propellants align with green and sustainable principles but face challenges such as long ignition delay times (t_{id}) or even non-hypergolic behavior, mainly due to the limited oxidizing ability of H_2O_2. The catalytic ignition concept of ionic liquids with HNO_3 for propellant applications was first demonstrated in 2010,[14] establishing the foundation for using catalysts to trigger IL combustion. Introducing catalysts to enhance the H_2O_2 decomposition to strongly oxidizing species, such as ·OH, $\cdot O_2^-$, and $^1O_2$, is the key to overcome the ignition problem.[15–18] In recent studies, the t_{id} of ILs-H_2O_2 has been found to be still too long for the catalytic ignition of propellants, such as $[N(CH_3)_4]_n(Cu_2I_3)_n$ and $[FcCH_2N(CH_3)_3]_2(Cu_2I_4)$, which give t_{id} values of 55 ms and 54 ms for $[EMIM][BH_3CN]$-H_2O_2, respectively.[19] The fixed electronic environment and strong ionic bonding in these compounds slow down the dissociation to release active radicals.[20–22] Moreover, their high-dimensional structures introduce significant steric hindrance that blocks active sites.[23–25] Therefore, more efficient catalysts are required to address the ignition challenge of the IL-H_2O_2 propellants.

Previous work has demonstrated that zero-dimensional complexes can significantly reduce the ignition delay time of [BMIM]DCA IL-H_2O_2 (t_{id} = 30 ms, Fig. 1). Low-dimensional metal complexes exhibit prolonged stable dispersion in ILs while facilitating the efficient decomposition of H_2O_2, thereby producing highly reactive oxygen species (ROS). The mechanism originates in the optimal d-orbital (metal)–LUMO (H_2O_2) overlap, highly reducing the O–O bond cleavage energy.[26–28] Exposing the active sites through the design of coordination-unsaturated, low-dimensional complexes further enhances the

[a]*College of Chemistry and Molecular Sciences, Henan University, Mingli Road North 379, 450046 Zhengzhou, China. E-mail: yqzhang@ipe.ac.cn*
[b]*Zhengzhou Institute of Emerging Industrial Technology, East Third Ring Road and Jincheng Avenue Intersection East 300 Meters, 450000, Zhengzhou, China*
[c]*Institute of Process Engineering, Chinese Academy of Sciences, Beiertiao 1#, Zhongguancun, Haidian District, 100190, Beijing, China*

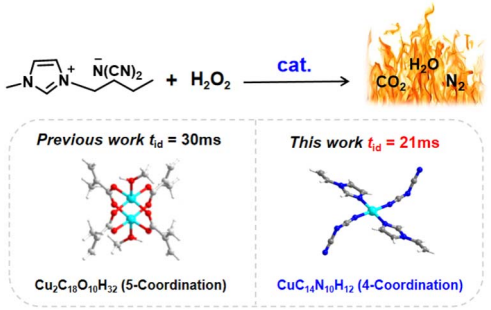

Fig. 1 Catalytic ignition of the [BMIM]DCA-H_2O_2 propellant.

electron transfer during H_2O_2 activation, achieving faster catalytic ignition.[29,30]

In this work, a series of metal complexes, M(vim)$_2$(DCA)$_2$ (M = Mn/Fe/Co/Cu, vim = vinylimidazole, and DCA = N(CN)$_2$), were synthesized. Cu(vim)$_2$(DCA)$_2$ exhibited the best catalytic performance with a minimum t_{id} value of 21 ms. Dynamic light scattering and UV-vis spectroscopy analyses confirmed the long-term stability of Cu(vim)$_2$(DCA)$_2$ dispersion in [BMIM]DCA. EPR spectroscopy revealed that H_2O_2 was catalyzed to generate ROS ($\cdot OH$, $\cdot O_2^-$ and $^1O_2$), which subsequently triggered rapid ignition through the reaction with [BMIM]DCA.

Experimental

Note! Chemical experiments require strict safety practices. Reagents must be handled carefully, and their properties must be understood beforehand. For example, in the IL-H_2O_2 ignition tests, although 98% H_2O_2 vapor is not significantly toxic, its strong oxidizing nature demands caution. Direct skin contact can damage cell structures and cause severe burns. When metal complexes are used to catalyze the IL-H_2O_2 reactions, there is also a risk of accidental ignition of flammable materials. H_2O_2 quantities must be strictly controlled, as excess can rapidly produce large gas volumes, potentially leading to explosions. Therefore, comprehensive safety measures must be implemented, including performing all operations in a functioning fume hood, wearing safety goggles, and preventing gas accumulation.

Materials

All chemicals were commercially available analytical grade reagents and were used without further purification. 1-Butyl-3-methylimidazolium dicyandiamide ([BMIM]DCA, 98%) was purchased from Shanghai Chengjie Chemical Co., Ltd. Manganese chloride ($MnCl_2$, 99%) was bought from Damas-Beta. Ferrous chloride ($FeCl_2$, 99.5%), copper chloride ($CuCl_2$, 98%), vinyl imidazole (vim, 99%), sodium dicyandiamide (NaDCA, 96%), and fluoroboric acid (HBF_4, 40%) were from Aladdin Company. Cobalt chloride ($CoCl_2$, 99.7%) was from Marklin. Triethylamine (TEA, 99%) was from General-Reagent. Hydrogen peroxide (H_2O_2, 98%) was purchased from Shanghai Xushi Science and Technology Co., Ltd.

Synthetic procedures

The synthesis of M(vim)$_2$(DCA)$_2$ (M = Mn, Fe, Co, and Cu) is illustrated in Fig. 2. The detailed procedures are as follows:

Mn(vim)$_2$(DCA)$_2$ complex. $MnCl_2$ (2 mmol, 0.252 g) was dissolved in H_2O (10 mL) with magnetic stirring. EtOH (10 mL) was added, and the mixture was heated. At 60 °C, vinylimidazole (4 mmol, 0.376 g) and 1.33 M NaDCA solution were added dropwise, followed by the addition of HBF_4 (200 μL) as an acid regulator. The reaction was kept at 60 °C for 2 h, then filtered to give a colourless solution. Colourless block crystals formed after standing at room temperature for 2 days.

Fe(vim)$_2$(DCA)$_2$ and Co(vim)$_2$(DCA)$_2$ complexes. These were prepared similarly to the Mn complex. $FeCl_2$ (2 mmol, 0.254 g) or $CoCl_2$ (2 mmol, 0.259 g) was dissolved in H_2O (10 mL), followed by the addition of EtOH (10 mL). The mixture was heated to 60 °C with stirring, then vinylimidazole (4 mmol, 0.376 g), 1.33 M NaDCA solution, and HBF_4 (200 μL) were added dropwise. After stirring at 60 °C for 2 h, the mixture was filtered while the solvent was still hot. The filtrate of Fe(vim)$_2$(DCA)$_2$ was colorless and that of Co(vim)$_2$(DCA)$_2$ was pink. After standing at room temperature for 2 days, colorless rod-like crystals (Fe) and orange block crystals (Co) were obtained.

Cu(vim)$_2$(DCA)$_2$ complex. $CuCl_2$ (2 mmol, 0.269 g) was dissolved in H_2O (10 mL). DMF (10 mL) was added, and the mixture was heated to 60 °C with magnetic stirring. At this temperature, vinylimidazole (4 mmol, 0.376 g) and 1.33 M NaDCA solution were added dropwise, followed by the addition of TEA (150 μL). The reaction was stirred at 60 °C for 2 h. After hot filtration, a clear blue filtrate was obtained. The blue needle-like crystals were formed after standing at room temperature for 2 days.

Characterization

Single crystal X-ray diffraction (SCXRD) data were collected on a Gemini E diffractometer with Mo Kα radiation ($\lambda = 0.71073$ Å). Data were processed using the Olex2 software to solve the structure. Powder X-ray diffraction (PXRD) patterns were recorded on a Rigaku/Smart Lab SE diffractometer using Cu Kα_1 and Co Kα_1 radiation, scanning from 5° to 50° at 10° min^{-1}. Phase purity was verified by comparison with the SCXRD-simulated patterns. Mixed fuels were prepared by blending 10 wt% catalyst with 90 wt% [BMIM]DCA for physicochemical tests and ignition evaluation. Thermal stability was assessed on a Mettler TGA3+ thermogravimetric analyzer under N_2

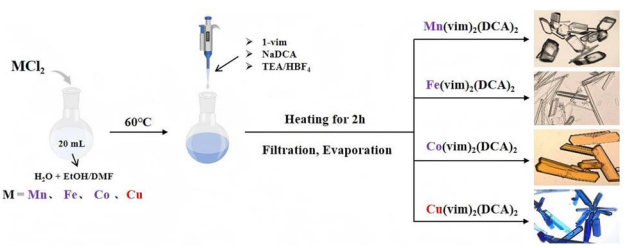

Fig. 2 Synthesis of the M(vim)$_2$(DCA)$_2$ (M = Mn, Fe, Co, and Cu) complexes.

atmosphere, heating from 50 °C to 800 °C at 10 °C min^{-1}. The heat of combustion (ΔH_c) was measured using an oxygen-bomb calorimeter. The long-term dispersion stability of the complexes in IL was studied using a Malvern Panalytical Zetasizer Pro particle-size analyzer and a Shimadzu UV-3600 PLUS spectrophotometer (scan range 240–800 nm). Ignition tests were recorded with a high-speed camera (OLYMPUS i-SPEED3, 1000 fps). Electron paramagnetic resonance (EPR) spectra were acquired on a Bruker EMXPlus-10/12 spectrometer to detect the reactive oxygen species. In addition, the formation enthalpy (ΔH_f) of each complex was computed using the CP2K 2023.1 method (see SI), from which the ΔH_f of the mixed fuel was derived. Specific impulse (I_{sp}) data for the [BMIM]DCA-H_2O_2 system with 10 wt% catalyst were calculated through the NASA-CEA program with an oxidizer-to-fuel (O/F) range of 0.5–6.

Results and discussion

Catalyst structures

The $M(vim)_2(DCA)_2$ (M = Mn, Fe, Co, and Cu) complexes were synthesized, and the crystallographic data are shown in Tables S1–S5. The complexes were characterized by FT-IR, PXRD and TG. In the FT-IR spectra (Fig. S1), the peak at 2173 cm^{-1} corresponds to C≡N of the DCA ligand. The peaks at 3137 cm^{-1}, 1358 cm^{-1}, and 1102 cm^{-1} are assigned to the unsaturated C–H stretching vibration, C–C/C–N skeleton stretching vibration, and C–H bending vibration of the imidazole ring, respectively. The peak at 1647 cm^{-1} represents the C=C stretching of the vinyl group on the imidazole ring. The PXRD patterns (Fig. S2) show that the experimental diffraction peaks match the simulated patterns, indicating high purity of the sample. TG curves (Fig. S3) show decomposition temperatures (T_d) of 186 °C (Mn), 218 °C (Fe), 218 °C (Co), and 202 °C (Cu), demonstrating their good thermal stabilities.

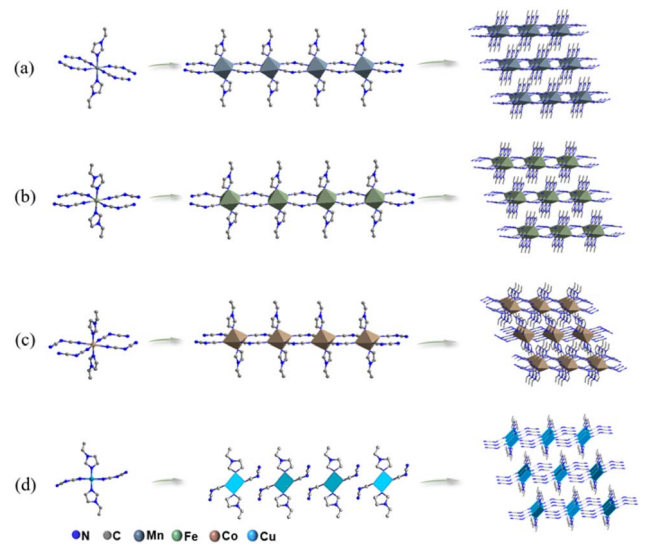

Fig. 3 Structures of (a) $Mn(vim)_2(DCA)_2$, (b) $Fe(vim)_2(DCA)_2$, (c) $Co(vim)_2(DCA)_2$, and (d) $Cu(vim)_2(DCA)_2$. Hydrogen atoms have been omitted for clarity.

The SCXRD structures of $M(vim)_2(DCA)_2$ (M = Mn, Fe, Co, and Cu) are shown in Fig. 3. The Mn and Fe complexes crystallize in the triclinic space group $P\bar{1}$, and the Co complex in the orthorhombic space group *Cmca*. They exhibit similar coordination patterns. Each M(II) center is coordinated by six N atoms in an octahedral geometry and linked *via* DCA bridges, forming one-dimensional (1D) chain structures. In $Mn(vim)_2(DCA)_2$, the Mn(II) ion coordinates with the N atom at the 3rd position of the imidazole ring in vim, and the Mn–N bond lengths are both 2.2 Å. The coordination environment of Mn(II) is the same as that of the N atom of C≡N in DCA, and the Mn–N bond length is 2.3 Å. The N–Mn–N bond angles vary from 87.9° to 180.0°. The C–N–Mn bond angles range from 126.5° to 163.1°. In $Fe(vim)_2(DCA)_2$, the Fe(II) ion coordinates with the N atom of the imidazole ring in vim, and the bond length is 2.2 Å. The Fe(II) ions alternately coordinate with the N atom of the C≡N group in DCA, and the bond length is 2.2 Å. The N–Fe–N bond angles range from 88.0° to 180.0°. The C–N–Fe bond angles range from 126.2° to 163.3°. In $Co(vim)_2(DCA)_2$, Co(II) forms a coordination bond with the N atom of the imidazole ring in vim, and the bond length is 2.1 Å. Co(II) forms a coordination bond with the N atom of the C≡N group in DCA, and the bond length is 2.1 Å. The N–Co–N bond angle ranges from 89.2° to 180.0°. The C–N–Co bond angles range from 126.7° to 160.8°.

$Cu(vim)_2(DCA)_2$, in the triclinic space group $P\bar{1}$, features a four-coordinate planar quadrilateral geometry, resulting in a zero-dimensional (0D) isolated molecule. Each asymmetric unit contains one M atom and two vim ligands. The N atoms at the symmetric positions of the Cu center are equivalent. There are two sets of bond lengths and bond angles of the same type. The Cu–N bond lengths are both 2.0 Å. The N–Cu–N bond angles of adjacent ligands are 90.2° and 89.8°, respectively, which are in proximity to a right angle. The N–Cu–N bond angles between the same ligands are both 180.0°, confirming a planar geometry. All structures assemble into three-dimensional networks *via* van der Waals interactions.

Physicochemical properties of the fuels (10 wt% complex + 90 wt% IL)

The $M(vim)_2(DCA)_2$ (M = Mn, Fe, Co, and Cu) complexes were ground into powder form in a mortar. For each complex, 0.02 g was added to [BMIM]DCA (0.18 g), and the mixture was ultrasonicated for 30 minutes to obtain a uniformly dispersed fuel. The properties of these fuels are summarized in Table 1.

After catalyst addition, the Cu-based fuel exhibits the highest T_d of 266.7 °C (Fig. 4a). The heat of combustion (ΔH_c) was measured by oxygen-bomb calorimetry (Fig. S5a), and the values for Mn-, Co-, and Cu-based mixed fuels are 29.6, 28.8, and 32.3 MJ kg^{-1}, respectively. The Fe-based sample could not be burned by O_2 during the test, and no relevant data were obtained. The ΔH_f of each mixed fuel was derived (Fig. 4b) through Table S6 and eqn (1)–(4) (SI), and the Cu-based mixed fuel shows the highest ΔH_f of 204.2 kJ mol^{-1}. Specific impulse (I_{sp}) was calculated using NASA-CEA with chamber pressure P_c = 300 psia and nozzle expansion ratio P_c/P_e = 20.4. Upon catalyst

Table 1 Physicochemical properties of the fuels (10 wt% catalyst + 90 wt% IL)

Propellant fuels	T_d[a] (°C)	ΔH_c[b] (MJ kg^{-1})	ΔH_f[c] (KJ mol^{-1})	I_{sp}[d] (s)	t_{id}[e] (ms)
[BMIM]DCA (IL)	288	—	245.0	267.5	No
Mn(vim)$_2$(DCA)$_2$ + IL	251	29.6	193.3	253.0	Bubble
Fe(vim)$_2$(DCA)$_2$ + IL	242	—	195.9	252.9	61
Co(vim)$_2$(DCA)$_2$ + IL	249	28.8	200.1	252.9	Bubble
Cu(vim)$_2$(DCA)$_2$ + IL	267	32.3	204.2	253.0	21

[a] Decomposition temperature. [b] Heat of combustion. [c] Formation enthalpies. [d] Specific impulse (O/F = 3.5, F is a mixed fuel and O is 98% H_2O_2). [e] Ignition delay time (average value of three tests).

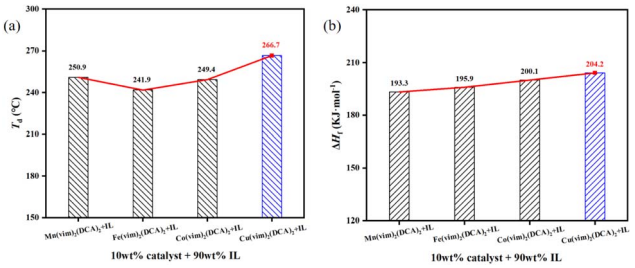

Fig. 4 (a) Decomposition temperature and (b) heat of formation of the fuels (10 wt% catalyst + 90 wt% IL).

addition, all mixed fuels exhibit a similar I_{sp} value of 253.0 s (O/F = 3.5, Fig. S5b), as the complexes share the same ligands.

Stability of 10 wt% complex in [BMIM]DCA

After ultrasonication, the mixed fuels are transparent liquids. To determine whether the complexes form colloidal dispersions or true solutions in [BMIM]DCA, Tyndall experiments were performed. As shown in Fig. 5 and Fig. S7, pure [BMIM]DCA shows no Tyndall effect, while all complexes + [BMIM]DCA mixtures exhibit clear Tyndall beams, confirming colloidal dispersion rather than dissolution.

Long-term dispersion stability was evaluated using dynamic light scattering (DLS) and UV-vis spectroscopy with Cu(vim)$_2$(DCA)$_2$ as an example. DLS (Fig. S8) shows that the particle sizes of Cu(vim)$_2$(DCA)$_2$ are 369.6 nm in [BMIM]DCA. UV-vis absorption spectra of M(vim)$_2$(DCA)$_2$ (M = Mn, Fe, Co, and Cu) + [BMIM]DCA mixtures are shown in Fig. 6 and S9. Compared to the solid-state UV-vis spectra of pure complexes (Fig. S4), the absorption bands of mixtures are red-shifted due to the solvation of [BMIM]DCA.[31,32] Strong absorption bands appear at 346 (Mn), 362 (Fe), 288 (Co), and 359 nm (Cu), assigned to the charge-transfer transitions of $\pi \rightarrow M(II)$.[33–36] The strong absorption bands were monitored over 25 days (seven measurements) and showed no significant changes in position or intensity, confirming the long-term dispersion stability of complexes in [BMIM]DCA.

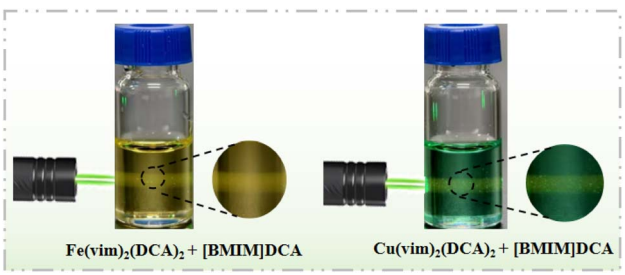

Fig. 5 Tyndall effect of Fe(vim)$_2$(DCA)$_2$ + IL and Cu(vim)$_2$(DCA)$_2$ + IL.

Ignition delay time measurements

Pure [BMIM]DCA and H_2O_2 are non-hypergolic. In the three-component system (IL; 98% and H_2O_2; catalyst), the ignition is primarily driven by the oxidizer H_2O_2. It means that the catalyst mainly promotes the decomposition of H_2O_2 into ROS, which then triggers the ignition with ionic liquid. The catalytic ignition performance of M(vim)$_2$(DCA)$_2$ in the [BMIM]DCA-H_2O_2 was evaluated by drop tests (Table 1). A droplet of mixed fuel (10 wt% complex + 90 wt% [BMIM]DCA) was dropped into a vial containing 1.5 mL of 98% H_2O_2. Ignition was recorded with a high-speed camera at 1000 fps. The ignition delay time (t_{id}) is defined as the interval from droplet-liquid contact to the appearance of an open flame, and values are the average of three tests. The results show that only rapid bubbling was

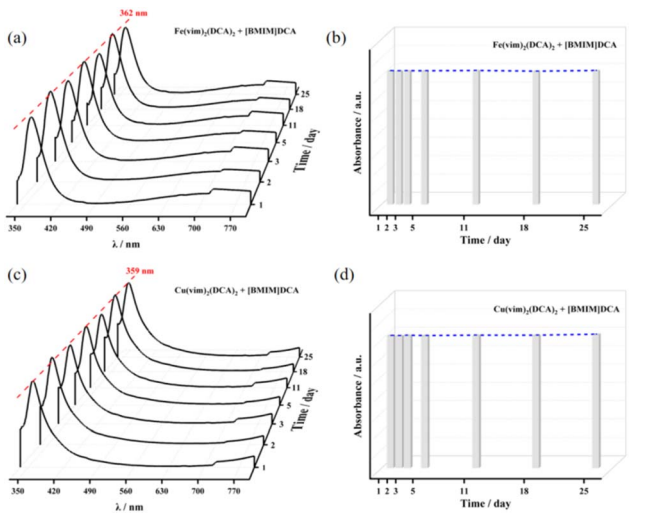

Fig. 6 (a) UV-vis spectrum of Fe(vim)$_2$(DCA)$_2$ + [BMIM]DCA. (b) Absorbance plot of Fe(vim)$_2$(DCA)$_2$ + [BMIM]DCA at 362 nm. (c) UV-vis spectrum of Fe(vim)$_2$(DCA)$_2$ + [BMIM]DCA. (d) Absorbance plot of Cu(vim)$_2$(DCA)$_2$ + [BMIM]DCA at 359 nm.

observed for Mn- and Co-based fuels. As shown in Fig. 7, the Fe-based fuel has an average t_{id} of 61 ms, with a standard deviation of ±1.0 ms. In comparison, $Cu(vim)_2(DCA)_2$ exhibits better catalytic performance with an average t_{id} of 21 ms and a standard deviation of ±0.5 ms.

Comparison of the t_{id} of IL-H_2O_2 between the reported and our catalysts is shown in Fig. 8. Iodine-containing catalysts, such as 10 wt% $[N(CH_3)_4]_n(Cu_2I_3)_n$ (t_{id} = 55 ms)[19] and 10 wt% $[FcCH_2N(CH_3)_3]_2(Cu_2I_4)$ (t_{id} = 54 ms)[19] in [EMIM][BH_3CN]-H_2O_2, were found to have relatively longer ignition delays. In these systems, iodine is believed to lower the Gibbs free energy of the reaction between H_2O_2 and [EMIM][BH_3CN], thereby promoting the reaction.[37,38] Several non-iodine catalysts have been reported with shorter ignition delays, including 10 wt% $Cu(AIM)_4(BH_3CN)_2$ (t_{id} = 37 ms),[39] 13 wt% $Cu_2[C(CH_3)COO]_4\cdot 2CH_3OH$ (t_{id} = 30 ms),[29] and 10 wt% $Cu(vim)_2(DCA)_2$ (t_{id} = 21 ms) in [EMIM][BH_3CN]/[BMIM]DCA-H_2O_2. The improved performance in these systems is generally attributed to Cu(II) directly catalyzing H_2O_2 decomposition to generate ROS, which enables rapid ignition with the ILs. In this work, low-dimensional coordination-unsaturated complexes, such as $Cu(vim)_2(DCA)_2$, offer fully exposed active sites. Concurrently, the vim ligand modulates the electron density of the metal center and facilitates direct H_2O_2 adsorption and activation, ultimately yielding faster ignition.

Analysis of the catalytic mechanism

EPR spectroscopy was applied to monitor the reactive oxygen species (ROS) generated during the catalytic process. For safety, tests were conducted using 30% H_2O_2. As shown in Fig. 9, the ROS (·OH, $\cdot O_2^-$, and $^1O_2$) produced upon catalysis by 10 wt% $Cu(vim)_2(DCA)_2$ + 90 wt% [BMIM]DCA were trapped with 5,5-dimethyl-1-pyrroline-*N*-oxide (DMPO) for ·OH/$\cdot O_2^-$ and 2,2,6,6-tetramethylpiperidine (TEMP) for $^1O_2$.[40–42] The lifetime of ·OH is very short (<1 μs) and its diffusion ability is limited, although it possesses the highly oxidizing ability.[43] In contrast, $\cdot O_2^-$ and $^1O_2$ have millisecond-scale lifetimes and can diffuse over longer distances, enabling sustained and effective reaction with

Fig. 7 Ignition delay times of (a) 10 wt% $Fe(vim)_2(DCA)_2$ + IL and (b) 10 wt% $Cu(vim)_2(DCA)_2$ + IL with H_2O_2 recorded using a high-speed camera (1000 fps).

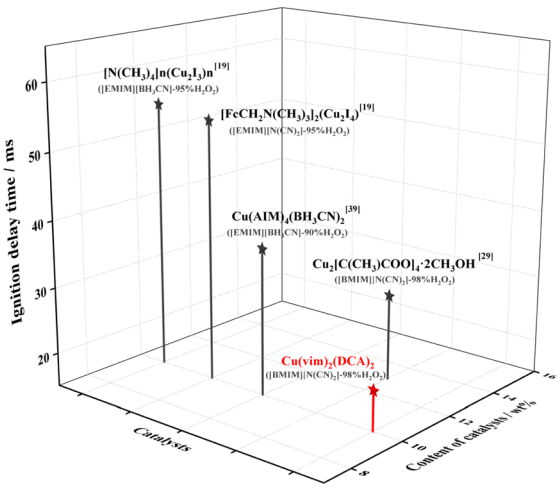

Fig. 8 Comparison of the t_{id} of IL-H_2O_2 with reported catalysts.

[BMIM]DCA.[44–46] Hence, $\cdot O_2^-$ and $^1O_2$ are considered the primary ROS responsible for the ignition of the [BMIM]DCA-H_2O_2 propellant.

To investigate the weak interactions in the $Cu(vim)_2(DCA)_2$ complex, an Independent Gradient Model (IGM) analysis was performed. Fig. 10a and S11 show the 3D structure of the complex from the top and side views. Green isosurfaces are clearly visible between the imidazole rings, which indicate the π–π stacking interactions. The electron distribution of $Cu(vim)_2(DCA)_2$ was then calculated (Fig. 10b), as the HOMO is mainly distributed on the ligand and the LUMO is located near the Cu site. In addition, the GAP value of the catalyst is only 0.306, and electron transfer in the catalyst is relatively facile,

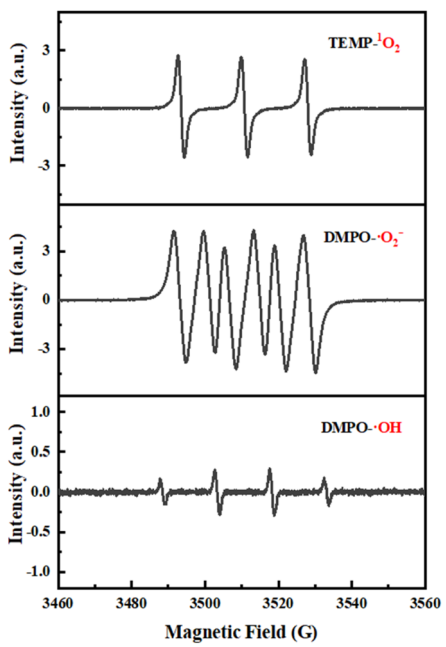

Fig. 9 Signals of the ROS (·OH, $\cdot O_2^-$ and $^1O_2$) during the catalytic decomposition of [BMIM]DCA-H_2O_2 by $Cu(vim)_2(DCA)_2$.

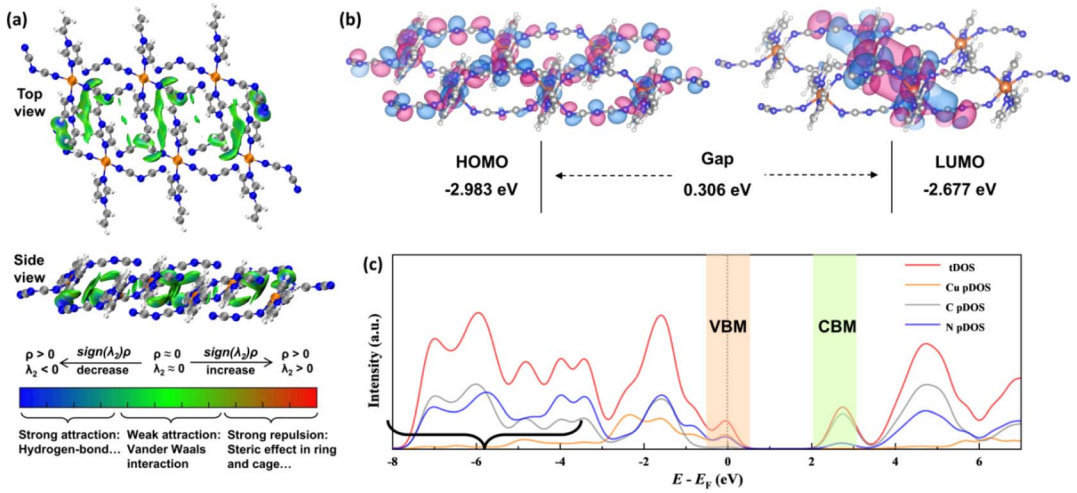

Fig. 10 (a) IGM isosurfaces of $Cu(vim)_2(DCA)_2$. (b) DFT-calculated HOMO and LUMO of $Cu(vim)_2(DCA)_2$. (c) Density of states of $Cu(vim)_2(DCA)_2$.

thereby promoting the catalytic activity at the Cu site. The density of states (DOS) calculations show that the Fermi level (E_F) is embedded into the valence band maximum (VBM), giving the complex metallic properties to some degree (Fig. 10c). This feature enables efficient electron transfer through π–π conjugation for the efficient activation of H_2O_2 during the catalytic process.

The catalytic activation of H_2O_2 by $Cu(vim)_2(DCA)_2$ is illustrated through a proposed cycle in Fig. 11a. The planar quadrilateral structure of $Cu(vim)_2(DCA)_2$ exposes the axial (*z*-direction) active sites of Cu(II). The process begins with H_2O_2 adsorption onto the Cu(II) center along the *z*-axis to form intermediate **I**. Subsequently, weak coordination of the second oxygen lone pair to Cu(II) yields intermediate **II**, followed by cleavage of the O–O bond to generate intermediate **III** containing two Cu–O bonds. One Cu–O bond then breaks, releasing a hydroxyl radical (·OH) and producing intermediate **IV**. The ·OH group participates in hydrogen bonding with another H_2O_2 molecule to form intermediate **V**. Subsequently, electron transfer within the H–O bond of H_2O_2 generates a proton, $\cdot O_2^-$ and $^1O_2$, thus forming intermediate **VI**. Cu(II)–H_2O releases a water molecule, and the catalyst returns to its original $Cu(vim)_2(DCA)_2$ structure.[29] The generated ROS (·OH, $\cdot O_2^-$, and $^1O_2$) attack the $[BMIM]^+$ and DCA^- ions of IL, and initiate chain-oxidation decomposition to CO_2, H_2O, N_2, thereby achieving rapid ignition.

Gibbs free energy of the catalytic ignition process was systematically studied by the DFT method (Fig. 11b). The results show that H_2O_2 was adsorbed onto the Cu site with an adsorption energy of −0.38 eV, forming hydrogen bonds with the N atoms of the ligand. The subsequent O–O bond cleavages to form 2 *OH with an energy barrier of 0.52 eV. After releasing one ·OH radical, a second H_2O_2 molecule interacts with the remaining *OH *via* hydrogen bonding. The hydrogen transfer from H_2O_2 to *OH occurs with a barrier of 0.40 eV and generates $*H_2O$ and *OOH. Finally, the desorption of H_2O regenerates the active catalytic sites. The unsaturated Cu center and electron-rich ligands improve the production of reactive oxygen species, resulting in the rapid ignition of the [BMIM]DCA-H_2O_2 propellant.

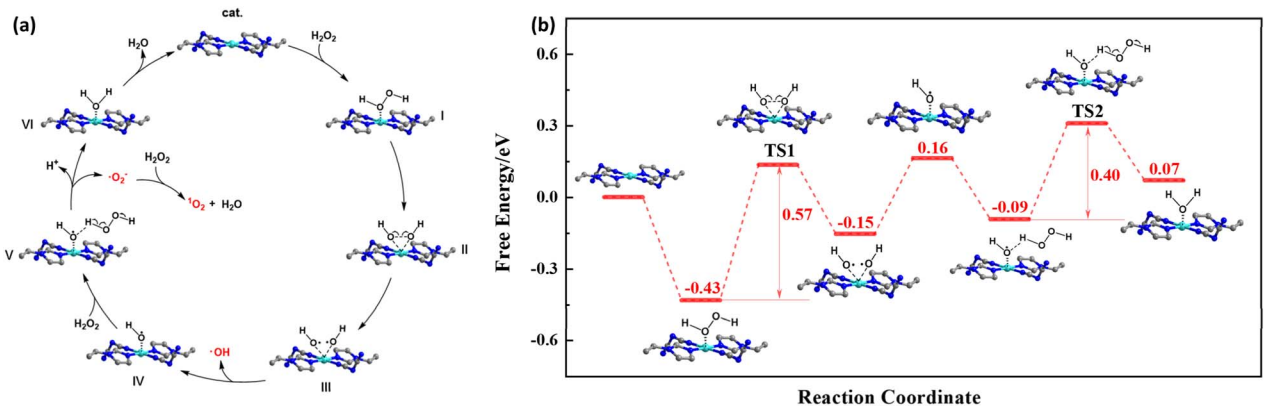

Fig. 11 (a) Proposed catalytic ignition process of $Cu(vim)_2(DCA)_2$ with H_2O_2. (b) Gibbs free energy changes in $Cu(vim)_2(DCA)_2$.

Conclusions

A series of complexes, $M(vim)_2(DCA)_2$ (M = Mn, Fe, Co, and Cu) catalysts, were synthesized. X-ray single crystal diffraction shows that the Mn, Fe, and Co complexes adopt 1D octahedral structures, while $Cu(vim)_2(DCA)_2$ is a 0D planar quadrilateral complex. The physicochemical properties of mixed fuels consisting of 10 wt% $M(vim)_2(DCA)_2$ and 90 wt% [BMIM]DCA were measured or calculated. The Cu-based mixed fuel exhibits comprehensive performance: T_d = 266.7 °C, ΔH_c = 32.3 MJ kg^{-1}, and ΔH_f = 204.2 KJ mol^{-1}. After the addition of the catalyst, all fuels exhibited similar specific impulse (I_{sp}) values (253 s, O/F = 3.5). Dispersion stability tests indicated that $Cu(vim)_2(DCA)_2$ forms a colloidal dispersion in [BMIM]DCA, and UV-vis spectroscopy confirmed the long-term stable dispersion of all complexes without sedimentation over 25 days. In catalytic ignition tests, $Cu(vim)_2(DCA)_2$ gave the shortest ignition time with t_{id} = 21 ms. EPR studies revealed that $Cu(vim)_2(DCA)_2$ catalyzes H_2O_2 to generate ·OH, $\cdot O_2^-$, and $^1O_2$, which subsequently trigger the rapid chemical ignition of [BMIM]DCA. This high activity was further investigated by DFT calculations. The zero-dimensional geometry of $Cu(vim)_2(DCA)_2$, with its unsaturated Cu center and electron-rich ligand framework, enables efficient electron transfer and promotes the generation of reactive oxygen species, leading to fast ignition. This work elucidates the pivotal role of the metal center in the IL-H_2O_2 system and offers valuable insights into the catalytic ignition of green propellants.

Author contributions

Yuqi Zhang: conceptualization, data curation, formal analysis, investigation, methodology, validation, visualization, and writing original draft. Yuan Yao: software, formal analysis, and visualization. Qing Cheng: supervision, resources, and writing – review and editing. Yanqiang Zhang: funding acquisition, project administration, resources, and writing – review and editing.

Conflicts of interest

The authors declare no conflict of interest.

Data availability

CCDC 2517002 {$Fe(vim)_2(DCA)_2$}, 2517003 {$Mn(vim)_2(DCA)_2$}, 2517004 {$Co(vim)_2(DCA)_2$} and 2517005 {$Cu(vim)_2(DCA)_2$} contain the supplementary crystallographic data for this paper.[47a–d] The data supporting this article have been included as part of the supplementary information (SI). Supplementary information: materials, computational methods, Fig. S1–S11, and Tables S1–S6. See DOI: https://doi.org/10.1039/d6ra00294c.

Acknowledgements

This work was supported by the National Natural Science Foundation of China (U21A20307 and 22178359) and the CAS Project for Young Scientists in Basic Research (YSBR-052).

Notes and references

1 F. S. Forbes, and P. A. Van Splinter, *Encyclopedia of Physical Science and Technology*, 2003, vol. 3, pp. 741–777.
2 S. M. Davis, and N. Yilmaz, *Advances in Aerospace Engineering*, 2014, p. 729313.
3 W. C. Keller, *Aviat., Space Environ. Med.*, 1988, **59**, A100–A106.
4 E. H. Vernot, J. D. Macewen, R. H. Bruner, C. C. Haun, E. R. Kinkead, D. E. Prentice, A. Hall, R. E. Schmidt, R. L. Eason, G. B. Hubbard and J. T. Young, *Fundam. Appl. Toxicol.*, 1985, **5**, 1050–1064.
5 W. Daimon, M. Tanaka and I. Kimura, *Symp. (Int.) Combust., [Proc.]*, 1985, **20**, 2065–2071.
6 A. Wilson, *2nd International Conference on Green Propellants for Space Propulsion*, ESA Special Publication, 2004, p. 557.
7 S. Schneider, T. Hawkins, M. Rosander, G. Vaghjiani, S. Chambreau and G. Drake, *Energy Fuels*, 2008, **22**, 2871–2872.
8 Q. Zhang and J. M. Shreeve, *Chem. Rev.*, 2014, **114**, 10527–10574.
9 I. I. Sam, S. Gayathri, G. Santhosh, J. Cyriac and S. Reshmi, *J. Mol. Liq.*, 2022, **350**, 118217.
10 R. Ciriminna, L. Albanese, F. Meneguzzo and M. Pagliaro, *Chemsuschem*, 2016, **9**, 3374–3381.
11 V. K. Bhosale, K. Lee, H. Yoon and S. Kwon, *Fuel*, 2024, **376**, 132688.
12 S. D. Rosenberg, *Acta Astronaut.*, 1982, **9**, 663–669.
13 K. R. Gagne, M. R. McDevitt and D. L. Hitt, *Aerospace*, 2018, **5**, 52.
14 J. L. Shamshina, M. Smiglak, D. M. Drab, T. G. Parker, H. W. H. Dykes, R. D. Salvo, A. J. Reich and R. D. Rogers, *Chem. Commun.*, 2010, **46**, 8965–8967.
15 Y. T. Zhang, X. Zhang, D. Y. Yin and Q. H. Zhang, *Molecules*, 2025, **30**, 1789.
16 V. K. Bhosale, J. Jeong, J. Choi, D. G. Churchill, Y. Lee and S. Kwon, *Combust. Flame*, 2020, **214**, 426–436.
17 Q. Cheng, Y. Q. Zhang, Y. Y. Cao, P. H. Dou, L. Liu and Y. Q. Zhang, *J. Mater. Chem. A*, 2025, **13**, 17434–17442.
18 K. L. Xie, X. Zhuang, X. Luo, Z. Y. Jing, X. Y. Song, A. Q. Hou and A. Q. Gao, *Green Chem.*, 2023, **25**, 4438–4445.
19 K. C. Wang, T. L. Liu, Y. H. Jin, S. Huang, N. Petrutik, D. Shem-Tov, Q. L. Yan, M. Gozin and Q. H. Zhang, *J. Mater. Chem. A*, 2020, **8**, 14661–14670.
20 Z. Li, X. Q. Qi, J. J. Wang, Z. Z. Zhu, J. X. Jiang, X. B. Niu, A. Cabot, J. S. Chen and R. Wu, *Susmat*, 2023, **3**, 498–509.
21 W. Liu, X. Q. Ding, J. J. Cheng, J. L. Jing, T. S. Li, X. Huang, P. P. Xie, X. C. Lin, H. L. Ding, Y. Kuang, D. J. Zhou and X. M. Sun, *Angew. Chem.*, 2024, **136**, e202406082.
22 P. Deshlahra, R. T. Carr and E. Iglesia, *J. Am. Chem. Soc.*, 2014, **136**, 15229–15247.

23 J. Ha, M. Jeon, J. Park, J. Kim and H. R. Moon, *Nanoscale Adv.*, 2023, **5**, 2111–2117.
24 C. Xu, M. He, B. B. Chen and B. Hu, *ACS Appl. Nano Mater.*, 2023, **6**, 17521–17530.
25 K. F. Yu, P. He, D. Zhang, H. Q. Wu, K. W. Shu, H. H. Long, Y. B. Sun, X. Pei, B. Jiang, K. C. Cao, Y. Li and L. J. Ma, *Angew. Chem., Int. Ed.*, 2025, **64**, e202511501.
26 P. Wu, F. F. Fang, J. S. Song, W. Peng, J. Liu, C. S. Li, Z. X. Cao and B. J. Wang, *J. Am. Chem. Soc.*, 2019, **141**, 19776–19789.
27 X. P. Zhang, A. Chandre, Y. M. Lee, R. Cao, K. Ray and W. Nam, *Chem. Soc. Rev.*, 2021, **50**, 4804–4811.
28 S. M. Adam, I. Garcia-Bosch, A. W. Schaefer, S. K. Sharma, M. A. Siegler, E. I. Solomon and K. D. Karlin, *J. Am. Chem. Soc.*, 2017, **139**, 472–481.
29 Q. Cheng, Y. Yao, P. H. Dou, L. Liu, Y. Y. Cao and Y. Q. Zhang, *J. Mater. Chem. A*, 2024, **12**, 21425–21433.
30 F. He, Y. N. Liu, X. Y. Peng, Y. Q. Chen, Q. Zheng, B. Yang, Z. J. Li, Q. Zhou, Q. H. Zhang, J. G. Lu, L. C. Lei, G. Wu and Y. Hou, *Nat. Commun.*, 2025, **16**, 6974.
31 C. H. Wang, W. Zhou, J. M. Ma, Z. Wang and C. Y. Zhang, *Molecules*, 2025, **30**, 2352.
32 J. Zhang, J. Yao and H. R. Li, *J. Phys. Chem. B*, 2022, **126**, 2279–2284.
33 C. A. Tibbetts, A. B. Wyatt, B. M. Luther, A. K. Rappé and A. T. Krummel, *J. Phys. Chem. B*, 2023, **127**, 932–943.
34 A. B. P. Lever, *J. Chem. Educ.*, 1974, **51**, 612–616.
35 M. Gras, N. Papaiconomou, E. Chainet and I. Billard, *Solvent Extr. Ion Exch.*, 2018, **36**, 583–601.
36 S. P. Devi, N. S. Devi, L. J. Singh, R. K. B. Devi, W. R. Devi, C. B. Singh and R. K. H. Singh, *Inorg. Nano-Met. Chem.*, 2017, **47**, 223–233.
37 F. A. S. Mota, L. H. Fei, C. L. Tang, Z. H. Huang and F. S. Costa, *Fuel*, 2022, **336**, 127086.
38 J. J. Pei, J. B. Liu, K. X. Fu, Y. K. Fu, K. Yin, S. L. Luo, D. Y. Yu, M. Y. Xing and J. M. Luo, *Nat. Commun.*, 2025, **16**, 800.
39 X. Zhao, Z. Wang, X. J. Qi, S. W. Song, S. Huang, K. C. Wang and Q. H. Zhang, *Inorg. Chem.*, 2021, **60**, 17033–17039.
40 A. J. Carmichael, L. Steelgoodwin, B. Gray and C. M. Arroyo, *Free Radical Res. Commun.*, 1993, **19**, S1–S16.
41 K. Reszka, P. Bilski and C. F. Chignell, *Free Radical Res. Commun.*, 1992, **17**, 377–385.
42 J. H. Wu, F. Chen, T. H. Yang and H. Q. Yu, *Proc. Natl. Acad. Sci. U. S. A.*, 2023, **120**, e2305706120.
43 J. W. E. Wilson, *J. Phys. Chem. Ref. Data*, 1972, **1**, 535–573.
44 M. G. Campo and J. R. Grigera, *J. Chem. Phys.*, 2005, **123**, 084507.
45 H. R. Yu, D. X. Liu, H. Y. Wang, H. S. Yu, Q. Y. Yan, J. H. Ji, J. L. Zhang and M. Y. Xing, *Chin. J. Catal.*, 2022, **43**, 2678–2689.
46 M. M. Islam, T. Imase, T. Okajima, M. Takahashi, Y. Niikura, N. Kawashima, Y. Nakamura and T. Ohsaka, *J. Phys. Chem. A*, 2009, **113**, 912–916.
47 (*a*) CCDC 2517002: Experimental Crystal Structure Determination, 2026, DOI: 10.5517/ccdc.csd.cc2qh4m0; (*b*) CCDC 2517003: Experimental Crystal Structure Determination, 2026, DOI: 10.5517/ccdc.csd.cc2qh4n1; (*c*) CCDC 2517004: Experimental Crystal Structure Determination, 2026, DOI: 10.5517/ccdc.csd.cc2qh4p2; (*d*) CCDC 2517005: Experimental Crystal Structure Determination, 2026, DOI: 10.5517/ccdc.csd.cc2qh4q3.